PCCP

ROYAL SOCIETY OF CHEMISTRY

PAPER

View Article Online
View Journal | View Issue

Cite this: *Phys. Chem. Chem. Phys.*, 2020, **22**, 2372

Characterizing local metallic bonding variation induced by external perturbation†

Hongwei Wang,[a] Jon Fuller,[a] Peng Chen,[a] Sergey I. Morozov [b] and Qi An *[a]

Received 2nd November 2019,
Accepted 3rd January 2020

DOI: 10.1039/c9cp05954g

rsc.li/pccp

The subtle variation of metallic bonding, induced by external influence, plays an essential role in determining physical, mechanical, and chemical properties of metals. However, it is extremely difficult to describe this variation because of the delocalization nature of metallic bonding. Here, we utilize the reduced density gradient and topological analysis of electron density to capture the local metallic bonding variations (LMBV) caused by lattice distortion and carrier injection in many face-centered cubic (fcc) metals. We find that the LMBV determines the traits of fcc metals such as strength, malleability, and ductility. Moreover, the fcc metals can become more flexible/stronger with the electron/hole injection, providing an important guidance to tune metals for desired mechanical properties.

1. Introduction

The response of metallic bonds to extrinsic perturbations, such as lattice strain,[1–3] point defect,[4,5] microstructure,[6] and charge transfer,[7] plays an essential role in the macroscopic performance of metals such as mechanical and catalytical performances. Previous studies indicated that charge transfer in the heteronuclear metal–metal bond of the bimetallic systems can effectively modify the surface electronic state and yield superior catalytic activity for energy-conversion.[2,7,8] Moreover, the intrinsic metallic bonding nature has a significant effect on the mechanical properties of metallic systems.[9–11] For example, Al[9] and Ir[12] exhibit an anomalous high ideal shear strength, due to their specific directional bonding feature which is different from many other metals. Therefore, it is important to understand the chemical and physical properties of metallic systems *via* the exploration of the bonding factors at an electronic level. However, the physical origin of metallic bonding is the electrostatic attractive force between delocalized electrons and positively charged metal ions;[13] making it extremely difficult to capture under external perturbations compared to the covalent bonding originated from orbital hybridization[14] and the ionic bonding described by Madelung theory.[15]

Bader developed an electronic charge theory in molecules which established a relationship between the solid-state structures and the topological properties of the relevant charge density.[16–18] It has been successfully employed to analyze the nature of bonding in a variety of solid-state systems and it is especially suitable for exploring the metallic systems. Furthermore, Johnson *et al.* proposed an effective method to describe some noncovalent interactions (NCIs) of the highly-delocalized and long-range characteristics that are usually not easy to identify due to the numerical noise.[19] They utilized a reduced density gradient (RDG), $\frac{1}{2(3\pi)^{1/3}}\frac{|\nabla\rho|}{\rho^{4/3}}$, the local deviation of the charge density from a homogeneous electron gas, to detect NCIs in real space, where ρ and $|\nabla\rho|$ denote the charge density and its gradient. The above NCIs index needs to be combined with the topological analysis of electron density[16] to classify whether the NCIs are attractive or repulsive.[17,18] Since this descriptor for NCIs could capture the bonding evolution based on the slight variation of charge density, it is qualified to survey the effects of some extrinsic perturbations on metallic systems.

To illustrate how subtle local metallic bonding variation (LMBV) influences the properties of metallic systems, we consider the mechanical deformation as the research subject due to its strong dependence upon the intrinsic bonding nature.[20] Recent studies have shown that the photoexcitation carriers such as the electron–hole pairs (EHPs)[21,22] can significantly modulate the mechanical properties in some ionic[21] or covalent inorganic semiconductors.[23] The altered chemical bonds by EHPs seriously reduce the energy barriers of deformation slip, which enhances the ductility of some brittle inorganic semiconductors under

[a] *Department of Chemical and Materials Engineering, University of Nevada-Reno, Reno, Nevada 89557, USA*
[b] *Department of Physics of Nanoscale Systems, South Ural State University, Chelyabinsk 454080, Russia. E-mail: qia@unr.edu*

† Electronic supplementary information (ESI) available: (i) Schematic illustration of supercell structure and Burgers vectors of deformation slip for fcc metals; (ii) reduced density gradient plot for the UST structure of fcc Au; (iii) graphic shown the relationship between RDG and the Laplacian charge density for fcc Au; (iv) GSFE curves of the twinning pathway for fcc metals; and (v) charge density analyses for the mechanical behaviors of fcc Pb; (vi) 2D and 3D negative Laplacian densities with reduced density gradient for deformed fcc Ir; and (vii) three-dimensional negative Laplacian density and reduced density gradient (RDG) for the deformed fcc Rh and Pt structures along the fault pathway. See DOI: 10.1039/c9cp05954g

light illumination.[22] However, it is unable to create the EHPs in metallic systems due to the lack of bandgap. Therefore, only the solely electron-charged or electron-deficient condition is considered to survey the carrier modified mechanical performance. Unlike the inorganic semiconductors in which the carriers prefer to be confined on the slip plane, the carriers in metallic systems are completely delocalized; it is therefore a challenge to identify how the carriers affect the mechanical properties. Hence it is expected to unveil the microscopic origin of the carrier modulated mechanical performances in metallic systems *via* the RDG[24] approach which is able to detect the subtle change of electrostatic interactions[19] by additional carriers.

2. Computational methods

The first-principles calculations were carried out based on the projector augmented wave (PAW) method[25] within the framework of generalized gradient approximation (GGA)[26] using the VASP package.[27,28] The planewave cutoff energy was set as 450 eV, and a Γ-centered $6 \times 6 \times 1$ k-point mesh was used for Brillouin zone integration. The energy and force convergence criterion for electronic and structural optimizations are 1×10^{-6} eV and 5 meV Å^{-1}. The crystal structure and reduced density gradient are visualized with the VESTA software.[29]

Here we take face-centered cubic (fcc) metals as the prototype metallic systems and examined Au, Pb, Ir, Pt, Rh, Ag, Pd, Ni, and Cu systems. The generalized stacking fault energy (GSFE) is calculated using the slab model in which parts of atomic layers were rigidly shifted by a displacement toward a specific direction on a particular lattice plane. The lattice constants for the fcc metals were optimized before constructing the slab models. The constructed supercell for the slab model should meet the periodic boundary condition. Since the crystal configuration for $\{111\}\langle 11\bar{2}\rangle$ slip breaks the mirror symmetry, the slab model with two stacking fault planes in the supercell is unable to accommodate the periodic boundary condition. As a result, the supercell has to include three slabs and three stacking fault planes, and three slabs are relatively displaced by a same amount toward three different but symmetry-equivalent with the $1/6a_0\langle 11\bar{2}\rangle$.[30] Fig S1 of ESI† displays the constructed supercell to accommodate the mechanical deformations as well as the sequential steps to generate stacking faults. The cell parameter and atomic position were only allowed to relax perpendicular to the slip plane in the GSFE calculations. Reduced density gradient and Laplacian of the density were analyzed using the critic2 code.[31]

The DFT simulations for electron and hole charged systems are carried out *via* modulating the total number of valence electrons. A homogeneous background-charge is automatically added to offset the unbalanced charge. It is possible to add or subtract a certain number of electrons and even fractional charge up to any specific carrier concentrations.

3. Results and discussion

In the following sections, we focus on the deformation slip of fcc metals, as well as the influence of the injected electron or hole carriers on their mechanical behaviors. The major operative slip system for fcc structures is the $\{111\}\langle 1\bar{1}0\rangle$ deformation slip[32] with the Burgers vector $\vec{b} = 1/2a_0\langle 1\bar{1}0\rangle$, where a_0 is the lattice constant of the conventional cubic structure. However, the $\{111\}\langle 1\bar{1}0\rangle$ deformation slip is energetically favorable

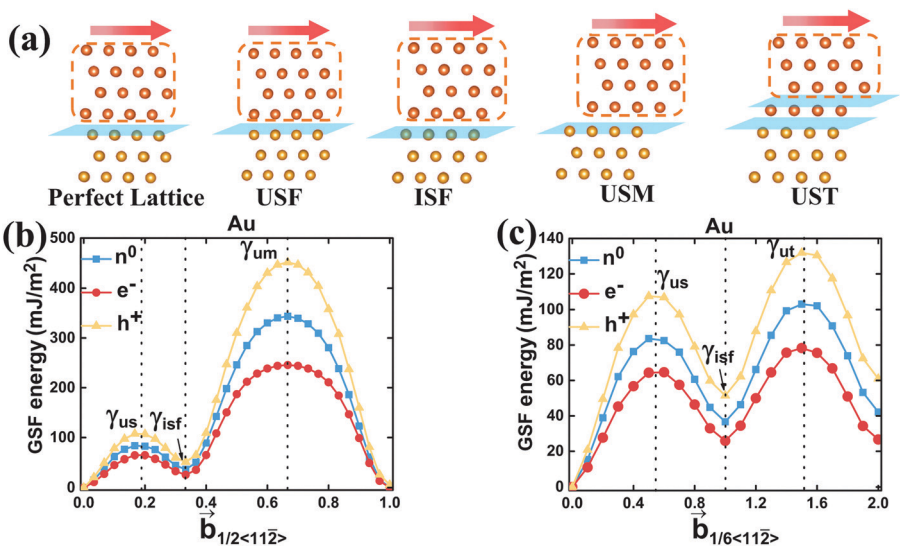

Fig. 1 (a) The schematic illustration of perfect lattice, unstable stacking fault (USF), intrinsic stacking fault (ISF), unstable maximum fault (USM), and unstable twinning fault (UST) for the $\{111\}\langle 11\bar{2}\rangle$ slip system of fcc Au. (b and c) Generalized stacking fault energy (GSFE) curves for the $\{111\}\langle 11\bar{2}\rangle$ slip system. The slip displacements along each pathway are given by the Burgers vectors of (b) a full dislocation $1/2\langle 11\bar{2}\rangle$, and (c) a Shockley partial dislocation $1/6\langle 11\bar{2}\rangle$. The twinning pathway (c) is proceeded by slipping the two parts of a crystal along a {111} lattice plane. The displacement $0 < |\vec{b}| < 1$ corresponding to the generation of an intrinsic stacking fault, followed by the displacement corresponding to the generation of an extrinsic stacking fault $1 < |\vec{b}| < 2$. The curves marked with n^0, e^-, and h^+ represent the deformation slips simulated at the neutral, one-electron charged, one-electron deficient states. The energy barriers for USF, ISF, USM, and UST are denoted as γ_{us}, γ_{us}, γ_{um}, and γ_{ut} respectively.

to dissociate into two partial slip systems[6] with Burgers vectors $1/6a_0\langle 2\bar{1}\bar{1}\rangle$ and $1/6a_0\langle 1\bar{2}1\rangle$ (symmetry equivalent with the $1/6a_0\langle 11\bar{2}\rangle$) to lower the misfit energy. Hence, only $\{111\}\langle 11\bar{2}\rangle$ slip system is selected to simulate deformation processing in the current study. The GSFE surfaces are calculated for two slip pathways:[33,34] one is to displace a half of a crystal on a $\{111\}$ slip plane with the full Burgers vector $\vec{b} = 1/2a_0\langle 11\bar{2}\rangle$, named as the fault pathway; the other is to slip a half of a crystal on a $\{111\}$ slip plane with the partial Burgers vector $\vec{b} = 1/6a_0\langle 11\bar{2}\rangle$ at first, then subsequently slip the crystal along the same partial direction on the adjacent $\{111\}$ plane, denoted as the twinning pathway. The fault and twinning pathways are two primary mechanisms to develop the plasticity in metals, which can generate dislocations and twins, respectively.

Fig. 1a illustrates the structural configurations of fcc Au at various stages of deformation slip. The GSFE curves of fcc Au for the fault and twinning pathways given in fractions of the magnitude of the Burgers vector are shown in Fig. 1b and c. The energy curves marked with the n^0, e^-, and h^+ represent GSFE calculated at neutral, one-electron charged, and one-electron deficient states, respectively. The charge density in our simulations is determined to be $\sim 10^{21}$ cm^{-3}. The two saddle and one valley points of the GSFE curve for the fault pathway are named as the unstable stacking fault (USF) energy, γ_{us}, the maximum unstable fault (USM) energy, γ_{um}, and the intrinsic stacking fault (ISF) energy, γ_{isf}, respectively. The energy barrier for nucleating the second stacking fault from the ISF structure along the twinning pathway, referred as the unstable twinning fault (UST) energy γ_{ut}. As shown in Fig. 1b and c, the whole GSFE profile of fcc Au is decreased with the injected electron and increased with the injected hole, indicating the availability of engineering mechanical performance with external carriers in metallic systems.

Since the deformation slip is accompanied by the chemical bond softening, breaking, or reforming,[35] it is necessary to survey the altered bonding feature in the deformation slip to understand how carriers modify the GSFE profile. Fig. 2a–c show the charge distributions of the perfect lattice, USF, and USM configurations for fcc Au surrounding the slip plane. The charge depletion between the adjacent nuclei occurs in USF structure in contrast to the perfect lattice and is further enhanced in the USM structure, which is responsible for the moderate and maximum values of γ_{us} and γ_{um} due to the gradually weakened metallic bonding. The charge distribution of the UST structure shown in Fig. S2 of ESI† is quite similar to that of USF structure, due to the closed local structure environments of USF and UST. The larger value of γ_{ut} than that of γ_{us} arises from the pre-nucleated ISF along the twinning pathway.

The evolution of metallic bonding in the deformation slip process can also be identified through the topology of the scalar field $\rho(r)$, which is given in terms of its critical points. The type of a critical point is classified with the number and sign of non-zero curvatures of $\rho(r)$. The curvatures of $\rho(r)$ correspond to eigenvalues in the diagonalization of the Hessian matrix of $\rho(r)$, the sum of which equal to the value of the quantity $\nabla^2\rho$ is detonated as the Laplacian of $\rho(r)$, $\nabla^2\rho = \lambda_1 + \lambda_2 + \lambda_3$, where λ_1, λ_2, and λ_3 are the three curvatures of $\rho(r)$ at the principal axes. A minimum critical point has positive curvatures in three principal axes, called a cage critical point (ccp), while a maximum critical point possesses three negative curvatures, which is named as a nuclear critical point (ncp). Moreover, the saddle critical points with two of the three curvatures negative and one of the three curvatures negative are termed as the bond critical point (bcp) and ring critical point (rcp) respectively. As shown in Fig. 2d–f, the critical points between two adjacent glide planes are calculated for the undeformed, USF, and USM structures of fcc Au. The coexisting bcps and rcps in the undeformed structure (Fig. 2d) indicate that both stronger two-center bonds and weaker multicenter bonds contribute to the atomic binding energy before the deformation.

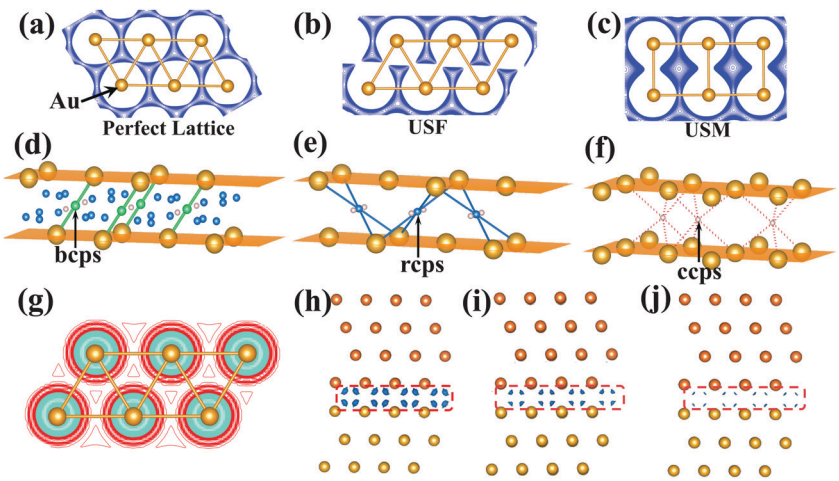

Fig. 2 Charge density $\rho(r)$ contour plot for fcc Au surrounding the slip plane for (a) perfect lattice, (b) USF, and (c) USM structures. The critical points (cps) characterizing the topology of a general scalar field $\rho(r)$ are illustrated for (d) perfect lattice, (e) USF, and (f) USM structures over the glide plane. The bond critical points (bcps), ring critical points (rcps), and cage critical points (ccps) with one positive and two negative, two positive and one negative, and three positive non-zero curvatures of $\rho(r)$ are represented with green, blue, and pink balls respectively. (g) The Laplacian density for USF structure of fcc Au. The cyan and red regions represent the negative and positive isosurfaces respectively. Non-covalent interactions on the slip plane for the USF structure at the (h) one-electron charged, (i) neutral, and (j) one-electron deficient states. The isosurface value of the plotted RDGs is 0.085.

In the USF structure, the bcps disappear on the glide plane and only the weaker four-center bonds featured by rcps produce the relevant binding energy (Fig. 2e), which leads to the increased systematic energy. The rcps are further removed by the lattice deformation on the glide plane of the USM structure, and only the ccps centered in the six-atom cage are left (Fig. 2f). These imply that all chemical bonds are broken across the glide plane, responsible for the maximum energy barrier of the USM structure. The results for the topology analysis of $\rho(r)$ are in consistency with the conclusion deduced from charge distributions.

In order to determine the microscopic origin of carrier modified GSFE profile, we characterized the local metallic bonding along slip planes using the RDG analysis which has the capacity of capturing the weak electrostatics in the low-density electron regions.[31] In contrast, the analysis of change density difference between the e^- and n^0 states and between the h^+ and n^0 states could not show any evident electronic transfer and redistribution on the slip plane, which is attributed to the delocalized character of conductive electrons in metallic systems.

The combination of RDG and ρ is able to roughly partition the different bonding regions in the real space: (1) high-RDG and low-ρ region corresponds to non-interacting density tails (such as lone pairs); (2) low-RDG and high-ρ region represents covalent bonds; and (3) low-RDG and low-ρ region refers to non-covalent interactions. Besides the RDG index, another important valuable NCI descriptor is the sign of the second largest eigenvalue λ_2 of the electron-density Hessian matrix at each isosurface point. Depending on the sign of λ_2, one can distinguish whether the classification of NCI is attractive ($\lambda_2 < 0$) or repulsive ($\lambda_2 > 0$).[18,36] The contour map of Laplacian of the density and RDG isosurfaces at the e^-, n^0, and h^+ states for the USF structure of fcc Au are shown in Fig. 2g–j. As illustrated in Fig. 2g, the sign of the Laplacian of the density is negative in a wide region surrounding the nuclei, indicating that the RDG near the nuclei should contribute to the attractive interaction. Moreover, it can be found obviously from Fig. 2h–j, the RDG mainly concentrates between the adjacent nuclei on the slip plane, in the region with negative sign of λ_2, suggesting that the LMBV plays an important role in determining the GSFE profile. The RDG profiles clearly fall within this spatial region, as shown in Fig. S3 of ESI.† The magnitude of RDG can be decreased/increased *via* the injected electron/hole, in contrast to the neutral state. As discussed above, the increased magnitude of RDG in the e^- state enhances the attractor between the adjacent nuclei on the slip plane, offsetting the charge depletion and strengthening metallic bonding in USF structure to lower the γ_{us}. Here the attractor, typically used in electronic structure topological analysis, represents the local maxima of reduced density gradient, indicating that the metallic bond has been found. Similarly, the decreased magnitude of RDG in the h^+ state weakens the attractor and softens metallic bonding on the slip plane, giving rise to the higher γ_{us}. This well explains how the injecting carriers affect the GSFE profile.

The RDG isosurfaces at the e^-, n^0, and h^+ states for the USM structure of fcc Au are plotted in Fig. 3a–c. The magnitude of RDG is obviously increased in the e^- state and decreased in the h^+ state for the USM structure, which is consistent with the analysis on the USF structure. However, the charge depletion on the slip plane in the USM structure is more serious than that in the USF structure, which causes the stronger LMBV due to the larger low-density regions of the USM structure (see Fig. 3). As a result, the stronger LMBV in the USM structure is more sensitive to the injected carriers in compare with that in the UST structure. That is why the change of γ_{um} with the injected carriers is much greater than that of γ_{us}. Therefore, the analysis of RDG well explains the microscopic origin of the carrier modified GSFE profile for fcc Au. Furthermore, the UST can be regarded as the combination of ISF and USF on the two adjacent planes,[37] meanwhile the ISF is much more energetically stable in contrast to USF, which induces weaker charge depletion and RDG. The major RDG of UST structure is localized on the subsequent stacking fault of the same character with USF, hence the analysis of charge distribution and LMBV is not employed for UST structure in the current work.

To extend our LMBV analysis on general metal systems. We applied it on other fcc metals: Pb, Ir, Pt, Rh, Ag, Pd, Ni, and Cu. The GSFE profiles of these metal systems for the fault pathway and

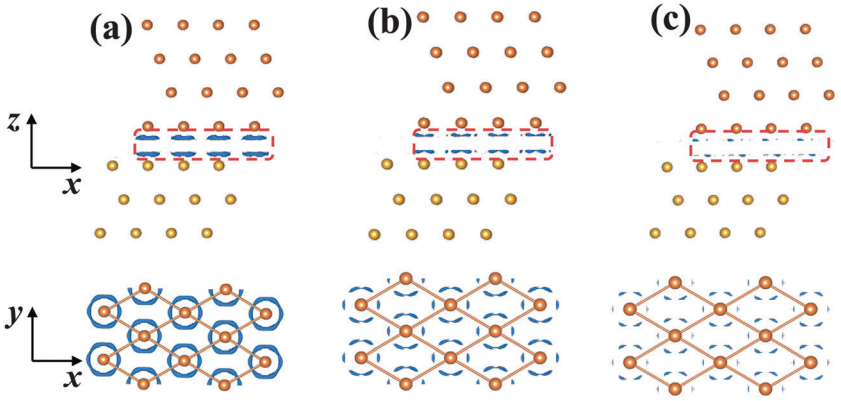

Fig. 3 Local metallic bonding variation on the slip plane for the USM structure at the (a) one-electron charged, (b) neutral, and (c) one-electron deficient states. The side and top views for the reduced density gradient are shown at the top and bottom. The isosurface value of the plotted RDGs is 0.085.

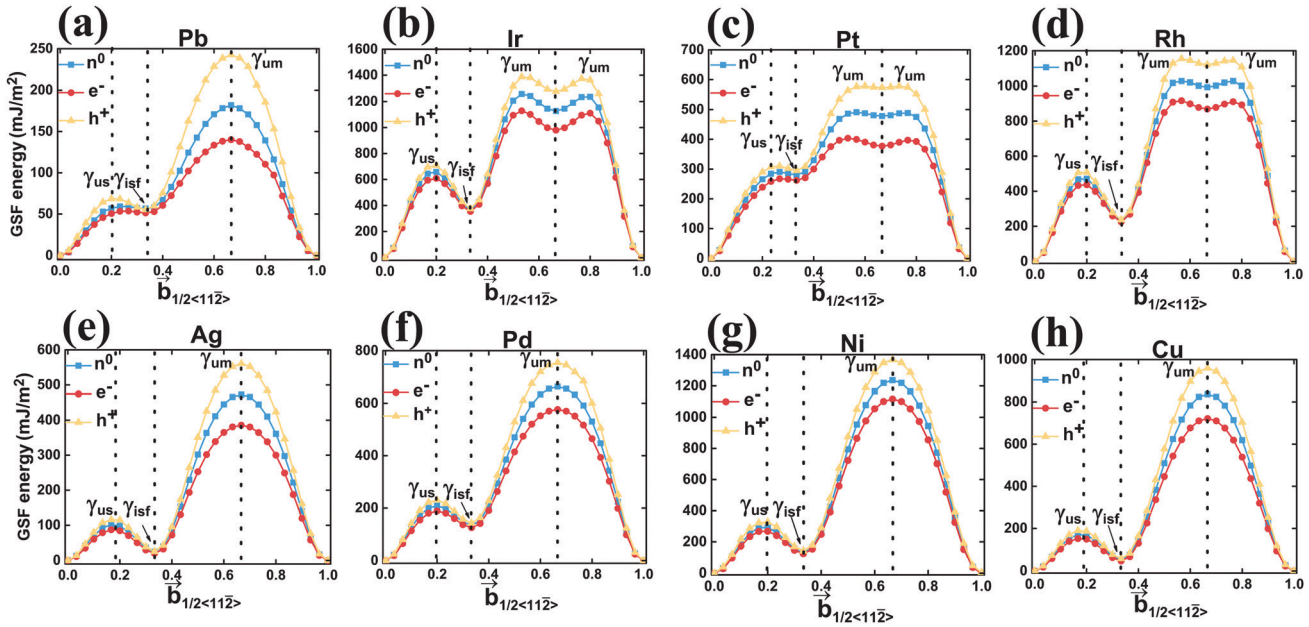

Fig. 4 GSFE curves for the fcc (a) Pb, (b) Ir, (c) Pt, (d) Rh, (e) Ag, (f) Pd, (g) Ni, and (h) Cu metals along $\{111\}\langle 11\bar{2}\rangle$ slip system. The slip displacement along each pathway is given by the Burgers vectors of $1/2\langle 11\bar{2}\rangle$. The symbols n^0, e^-, and h^+ represent the neutral, one-electron charged, one-electron deficient states.

twinning pathway are shown in Fig. 4 and Fig. S4 (ESI†). It should be noted that all these fcc metals display the same increased/decreased tendency for the GSFE profiles as the Au under the injected hole/electron conditions. This indicates the phenomenon of the carrier modified mechanical performance for fcc Au also exists in all other fcc metals which become more flexible or strong *via* electron or hole injection. We also perform the analysis of charge distribution and RDG for fcc Pb, which are shown in Fig. S5 and S6 (ESI). The same scenario as fcc Au appears: the intermediate fcc Pb structures in the deformation slip process with more charge depletion gives rise to the larger RDG and the higher energy barrier is more sensitive to the injected carriers. Interestingly, there is a small valley instead of peak at the partial Burgers vector of $2/3a_0\langle 11\bar{2}\rangle$ on the GSFE curves of fcc Ir, Pt, and Rh for the fault pathway. In order to explain this unusual phenomenon, we performed the analysis of Laplacian of the density and RDG for fcc Ir structures at the neutral state (Fig. S7, ESI†), with the energy barriers corresponding to the maximum peak and small valley of the GSFE curve. As illustrated in Fig. S7 (ESI†), the outmost electrons of fcc Ir situate at the localized d orbitals, and the directional character of d electron leads to the strong anisotropic RDG distribution.[12,38] This makes the attractive interaction lie outside the metallic bonding direction on the slip plane that leads to the maximum energy barrier of deformation slip in fcc Ir. However, the attractive interaction is well localized in metallic bonding region on the slip plane for the deformed structure with the partial Burgers vector of $2/3a_0\langle 11\bar{2}\rangle$. The RDG profiles of Pt and Rh show similar trends as Ir, as shown in Fig. S8 (ESI†). The above mechanism accounts for the unusual GSFE profile of fcc Ir, Pt, and Rh, and once again proves the RDG analysis can well describe the subtle change of bonding interaction in metallic system.

Finally, we briefly discuss the carrier modified deformation mechanism for fcc Al, which is different from other fcc metals. Previous studies indicated that the metallic bonds in fcc Al exhibit the obviously angular character, and the directional bonds are difficult to be reformed *via* charge redistributions under deformation.[9,10] As a result, fcc Al possesses a stronger ideal shear strength, compared to fcc Cu with the isotropic "sphere-in-glue" like bonds.[9] The localization of carriers on the slip plane forms the low-RDG and high-ρ environment (Fig. 5), displaying the covalent character to modify the GSFE profiles. The GSFE profiles of fcc Al for both fault and twinning pathways are shown in Fig. 5a and b, which exhibit the same variation tendency with injected carriers, like other fcc metals. The energy barriers of the intermediate structures in the deformation process are also proportion to the charge depletion on the slip plane (Fig. 5c). However, the mechanism of carrier modified GSFE profile for fcc Al is different from other metals, due to its directionally bonding feature. The injected carriers prefer to be localized on the slip plane instead of delocalization over the whole system. This is illustrated through the charge density difference between the e^- and n^0 states for USF and USM structures (Fig. 5d and e). The USM structure with more charge depletion is likely to accumulate more carriers, which is proportional to the relevant covalent bonds and energy barriers of the deformation slip (Fig. 5e).

4. Conclusions

In summary, the subtle LMBV in metallic systems has a significant effect on their mechanical properties, which can be characterized and explained by the RDG analysis. To validate this, the GSFE profiles for a series of fcc metals are calculated at the neutral, electron charged, and electron deficient states by first-principles simulations. We find that the energy barrier for

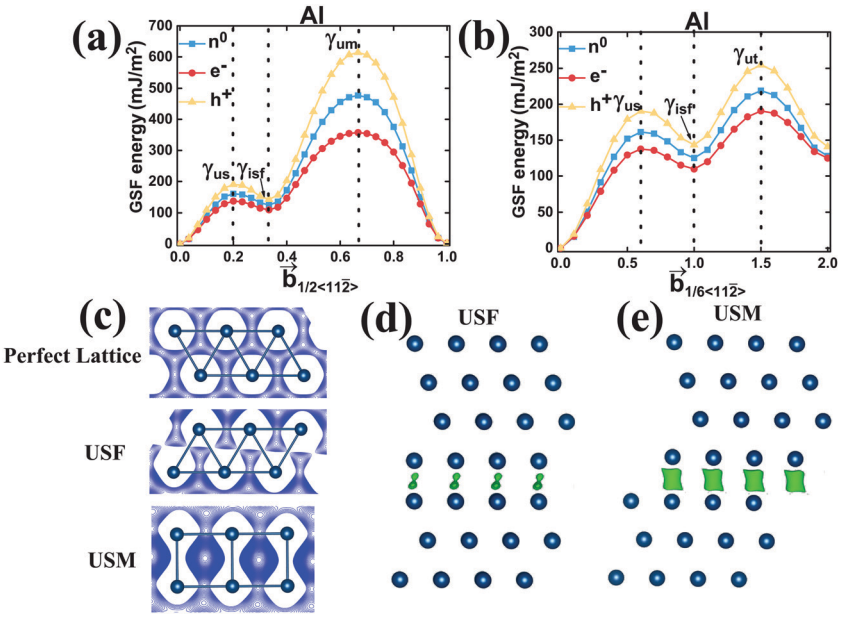

Fig. 5 GSFE curves of Al with (a) slip and (b) twinning pathways given as a function of the magnitude of the Burgers vectors of a full dislocation 1/2⟨11$\bar{2}$⟩, and a Shockley partial dislocation 1/6⟨11$\bar{2}$⟩. (c) Charge density contour plot for fcc Al surrounding the glide plane for perfect lattice, USF structure, and USM structure. Charge density difference between the neutral and one-electron charged states for the (d) USF and (e) USM structures.

deformation slip in fcc metals can be obviously decreased/increased *via* the injected electron/hole, anticipated to become more flexible/stronger. Our study not only provides an effective strategy to investigate the response of metallic bonding interactions due to some external influences, such as element doping, grain boundary, pressure, and injected carrier, but also offers a practical way for controlling the toughness or flexible extent in metallic systems.

Conflicts of interest

There are no conflicts to declare.

Acknowledgements

This work was supported by the National Science Foundation (CMMI-1727428) and US Nuclear Regulatory Commission (NRC-HQ-84-15-G-0028). SM was thankful for the support by Act 211 Government of the Russian Federation, under No. 02.A03.21.0011 and by the Supercomputer Simulation Laboratory of South Ural State University.

References

1 M. Mavrikakis, B. Hammer and J. K. Nørskov, Effect of Strain on the Reactivity of Metal Surfaces, *Phys. Rev. Lett.*, 1998, **81**, 2819.
2 J. R. Kitchin, J. K. Nørskov, M. A. Barteau and J. Chen, Role of Strain and Ligand Effects in the Modification of the Electronic and Chemical Properties of Bimetallic Surfaces, *Phys. Rev. Lett.*, 2004, **93**, 156801.
3 P. Strasser, S. Koh, T. Anniyev, J. Greeley, K. More, C. Yu, Z. Liu, S. Kaya, D. Nordlund and H. Ogasawara, Lattice-Strain Control of the Activity in Dealloyed Core–Shell Fuel Cell Catalysts, *Nat. Chem.*, 2010, **2**, 454.
4 M. Muzyk, D. Nguyen-Manh, K. Kurzydłowski, N. Baluc and S. Dudarev, Phase Stability, Point Defects, and Elastic Properties of Wv and W-Ta Alloys, *Phys. Rev. B: Condens. Matter Mater. Phys.*, 2011, **84**, 104115.
5 P. Olsson, T. Klaver and C. Domain, Ab Initio Study of Solute Transition-Metal Interactions with Point Defects in Bcc Fe, *Phys. Rev. B: Condens. Matter Mater. Phys.*, 2010, **81**, 054102.
6 D. Hull and D. J. Bacon, *Introduction to Dislocations*, Butterworth-Heinemann, 2001.
7 J. A. Rodriguez and D. W. Goodman, The Nature of the Metal-Metal Bond in Bimetallic Surfaces, *Science*, 1992, **257**, 897–903.
8 J. Greeley and M. Mavrikakis, Alloy Catalysts Designed from First Principles, *Nat. Mater.*, 2004, **3**, 810.
9 S. Ogata, J. Li and S. Yip, Ideal Pure Shear Strength of Aluminum and Copper, *Science*, 2002, **298**, 807–811.
10 P. N. Nakashima, A. E. Smith, J. Etheridge and B. C. Muddle, The Bonding Electron Density in Aluminum, *Science*, 2011, **331**, 1583–1586.
11 S. Ogata, J. Li, N. Hirosaki, Y. Shibutani and S. Yip, Ideal Shear Strain of Metals and Ceramics, *Phys. Rev. B: Condens. Matter Mater. Phys.*, 2004, **70**, 104104.
12 S. Kamran, K. Chen, L. Chen and L. Zhao, Electronic Origin of Anomalously High Shear Modulus and Intrinsic Brittleness of Fcc Ir, *J. Phys.: Condens. Matter*, 2008, **20**, 085221.
13 G. Grimvall, B. Magyari-Köpe, V. Ozoliņš and K. A. Persson, Lattice Instabilities in Metallic Elements, *Rev. Mod. Phys.*, 2012, **84**, 945.

14 V. L. Deringer, A. L. Tchougréeff and R. Dronskowski, Crystal Orbital Hamilton Population (Cohp) Analysis as Projected from Plane-Wave Basis Sets, *J. Phys. Chem. A*, 2011, **115**, 5461–5466.
15 K. Ragavendran, D. Vasudevan, A. Veluchamy and B. Emmanuel, Computation of Madelung Energies for Ionic Crystals of Variable Stoichiometries and Mixed Valencies and Their Application in Lithium-Ion Battery Voltage Modeling, *J. Phys. Chem. B*, 2004, **108**, 16899–16903.
16 R. F. Bader and H. Essén, The Characterization of Atomic Interactions, *J. Chem. Phys.*, 1984, **80**, 1943–1960.
17 R. F. Bader, A Quantum Theory of Molecular Structure and Its Applications, *Chem. Rev.*, 1991, **91**, 893–928.
18 R. F. Bader, A Bond Path: A Universal Indicator of Bonded Interactions, *J. Phys. Chem. A*, 1998, **102**, 7314–7323.
19 A. Otero-de-la-Roza, E. R. Johnson and J. Contreras-García, Revealing Non-Covalent Interactions in Solids: Nci Plots Revisited, *Phys. Chem. Chem. Phys.*, 2012, **14**, 12165–12172.
20 S. Ogata, Y. Umeno and M. Kohyama, First-Principles Approaches to Intrinsic Strength and Deformation of Materials: Perfect Crystals, Nano-Structures, Surfaces and Interfaces, *Modell. Simul. Mater. Sci. Eng.*, 2008, **17**, 013001.
21 Y. Oshima, A. Nakamura and K. Matsunaga, Extraordinary Plasticity of an Inorganic Semiconductor in Darkness, *Science*, 2018, **360**, 772–774.
22 H. Wang, S. I. Morozov, W. A. Goddard III and Q. An, Light Irradiation Induced Brittle-to-Ductile and Ductile-to-Brittle Transition in Inorganic Semiconductors, *Phys. Rev. B*, 2019, **99**, 161202.
23 P. G. Callahan, B. B. Haidet, D. Jung, G. G. Seward and K. Mukherjee, Direct Observation of Recombination-Enhanced Dislocation Glide in Heteroepitaxial Gaas on Silicon, *Phys. Rev. Mater.*, 2018, **2**, 081601.
24 E. R. Johnson, S. Keinan, P. Mori-Sánchez, J. Contreras-García, A. J. Cohen and W. Yang, Revealing Noncovalent Interactions, *J. Am. Chem. Soc.*, 2010, **132**, 6498–6506.
25 P. E. Blöchl, Projector Augmented-Wave Method, *Phys. Rev. B: Condens. Matter Mater. Phys.*, 1994, **50**, 17953.
26 J. P. Perdew, K. Burke and M. Ernzerhof, Generalized Gradient Approximation Made Simple, *Phys. Rev. Lett.*, 1996, **77**, 3865.
27 G. Kresse and J. Hafner, Ab Initio Molecular Dynamics for Liquid Metals, *Phys. Rev. B: Condens. Matter Mater. Phys.*, 1993, **47**, 558.
28 G. Kresse and D. Joubert, From Ultrasoft Pseudopotentials to the Projector Augmented-Wave Method, *Phys. Rev. B: Condens. Matter Mater. Phys.*, 1999, **59**, 1758.
29 K. Momma and F. Izumi, Vesta 3 for Three-Dimensional Visualization of Crystal, Volumetric and Morphology Data, *J. Appl. Crystallogr.*, 2011, **44**, 1272–1276.
30 A. Nakamura, M. Ukita, N. Shimoda, Y. Furushima, K. Toyoura and K. Matsunaga, First-Principles Calculations on Slip System Activation in the Rock Salt Structure: Electronic Origin of Ductility in Silver Chloride, *Philos. Mag.*, 2017, **97**, 1281–1310.
31 A. Otero-de-la-Roza, E. R. Johnson and V. Luaña, Critic2: A Program for Real-Space Analysis of Quantum Chemical Interactions in Solids, *Comput. Phys. Commun.*, 2014, **185**, 1007–1018.
32 P. M. Anderson, J. P. Hirth and J. Lothe, *Theory of Dislocations*, Cambridge University Press, 2017.
33 Z. Jin, S. Dunham, H. Gleiter, H. Hahn and P. A. Gumbsch, Universal Scaling of Planar Fault Energy Barriers in Face-Centered Cubic Metals, *Scr. Mater.*, 2011, **64**, 605–608.
34 S. Schönecker, X. Li, M. Richter and L. Vitos, Lattice Dynamics and Metastability of Fcc Metals in the Hcp Structure and the Crucial Role of Spin-Orbit Coupling in Platinum, *Phys. Rev. B: Condens. Matter Mater. Phys.*, 2018, **97**, 224305.
35 N. De Leon, X.-X. Yu, H. Yu, C. R. Weinberger and G. B. Thompson, Bonding Effects on the Slip Differences in the B 1 Monocarbides, *Phys. Rev. Lett.*, 2015, **114**, 165502.
36 G. Saleh, C. Gatti, L. Lo Presti and J. Contreras-García, Revealing Non-Covalent Interactions in Molecular Crystals through Their Experimental Electron Densities, *Chem. – Eur. J.*, 2012, **18**, 15523–15536.
37 E. B. Tadmor and S. Hai, A Peierls Criterion for the Onset of Deformation Twinning at a Crack Tip, *J. Mech. Phys. Solids*, 2003, **51**, 765–793.
38 S. Kamran, K. Chen and L. Chen, Ab Initio Examination of Ductility Features of Fcc Metals, *Phys. Rev. B: Condens. Matter Mater. Phys.*, 2009, **79**, 024106.

